



## Validation of multispectral imaging for the detection of selected adulterants in turmeric samples



Wele Gedara Chaminda Bandara<sup>a,\*</sup>, Gode Withanage Kasun Prabhath<sup>a</sup>, Dissanayake Walawwe Sahan Chinthana Bandara Dissanayake<sup>a</sup>, Vijitha Rohana Herath<sup>a</sup>, Gunawath Mudiyanselage Roshan Indika Godaliyadda<sup>a</sup>, Mervyn Parakrama Bandara Ekanayake<sup>a</sup>, Dhanushika Demini<sup>b</sup>, Terrence Madhujith<sup>b</sup>

<sup>a</sup> Department of Electrical and Electronic Engineering, Faculty of Engineering, University of Peradeniya, Peradeniya, 20400, Sri Lanka

<sup>b</sup> Department of Food Science and Technology, Faculty of Agriculture, University of Peradeniya, Peradeniya, 20400, Sri Lanka

### ARTICLE INFO

**Keywords:**  
Food quality  
Multispectral imaging  
Image understanding  
Adulteration of spices  
Statistical estimation  
Optical quality assessment

### ABSTRACT

Turmeric (*Curcuma longa*), is a popular spice in traditional cuisine and now is globally available. As in the case of many widespread spices, turmeric powder is often adulterated using various additives and colorants. Therefore, the identification of adulterated turmeric is of paramount importance. However, the existing methods are laborious, expensive and time-consuming. In this study, we propose a multispectral imaging system for detecting the percentage of the common adulterant; tartrazine colored rice flour found in turmeric powder. A multispectral imaging system was developed utilizing nine spectral bands with peak wavelengths from 405 nm to 950 nm. An algorithm was developed based on Principal Component Analysis (PCA) and Bhattacharyya Distance. The relationship between the Bhattacharyya Distance and the adulteration level was modeled as a second-order polynomial with an  $R^2 = 0.9911$  and the results were validated using an independent set of samples with an  $R^2 = 0.9816$ .

### 1. Introduction

Turmeric (*Curcuma longa*) has been used all over the world as a spice and an antimicrobial agent since antiquity. It has also been used in traditional medicine for thousands of years in different parts of the world. Curcumin (diferuloylmethane) (Jayaprakash et al., 2002) present in turmeric has been used extensively in Ayurvedic medicine for centuries because of its proven bioactivities such as its antioxidant (Ruby et al., 1995), analgesic, anti-inflammatory (Joe et al., 2004), antiseptic (Naz et al., 2010), and anticarcinogenic qualities (Chainani-wu NitaD.M. and M.P., 2003; Duvoix et al., 2005). Hence, there is a growing demand for turmeric in international trade because of its high popularity. Due to these reasons, turmeric powder has been often adulterated to obtain undue profits (Lotlikar Chindarkar, 2018; Daniells, 2018).

Materials such as rice flour, wheat flour, starch and chalk dust stained with different dyes and colorants are commonly added to

turmeric powder. Among these colorants, tartrazine (synthetic lemon yellow azo dye, E number: 102,  $C_{16}H_9N_4Na_3O_2S_2$ ), metanil yellow (yellow azo dye:  $C_{18}H_{14}N_3NaO_3S$ ) and lead chromate ( $PbCrO_4$ ) are the most commonly used colors (Bhatt, 2015; Dhakal et al., 2016; Shah, 2017; Screening and Spectroscopy). There have been instances where fabric and other industrial dyes and stains have also been used to adulterate turmeric powder.

A variety of conventional methods have been effectively used to detect the presence of adulterants in turmeric powder such as rapid color test (Shah, 2017), microscopic analysis (van Raamsdonk, 2015) and thin layer chromatography (Sen et al., 1974). Similarly, other methods such as high-performance liquid chromatography (Shah, 2017; Ashok et al., 2015; Fuh and Chia, 2002), micellar chromatographic method, and high-performance capillary electrolysis have been used to determine the presence of metanil yellow and aniline dyes. Despite the high accuracy and satisfactory detection limits, these conventional methods are limited as field deployable technology due to their

\* Corresponding author.

E-mail addresses: [chaminda.bandara@eng.pdn.ac.lk](mailto:chaminda.bandara@eng.pdn.ac.lk) (W.G. Chaminda Bandara), [gwkprabhath@eng.pdn.ac.lk](mailto:gwkprabhath@eng.pdn.ac.lk) (G.W. Kasun Prabhath), [sahan.dissanayake@eng.pdn.ac.lk](mailto:sahan.dissanayake@eng.pdn.ac.lk) (D.W. Sahan Chinthana Bandara Dissanayake), [vijitha@eng.pdn.ac.lk](mailto:vijitha@eng.pdn.ac.lk) (V.R. Herath), [roshangodd@ee.pdn.ac.lk](mailto:roshangodd@ee.pdn.ac.lk) (G.M. Roshan Indika Godaliyadda), [mpb.ekanayake@ee.pdn.ac.lk](mailto:mpb.ekanayake@ee.pdn.ac.lk) (M.P. Bandara Ekanayake), [deminismd@gmail.com](mailto:deminismd@gmail.com) (D. Demini), [tmadhujith@gmail.com](mailto:tmadhujith@gmail.com) (T. Madhujith).

operational complexity, destructive nature, extensive sample preparation, the requirement of chemicals and difficulty in automating the detection process. Moreover, most of these chemical analyses focus on the identification of the presence of a limited number of stains or colorants at a time.

In this light, hyperspectral and multispectral imaging are becoming increasingly popular for quality assessment of foods due to the limitations of traditional methods. Therefore, variety of hyperspectral and multispectral imaging systems and image processing algorithms have been developed to identify the presence of adulterants in various foods and food products such as meat, honey, sauce, spices, etc. In Shafiee et al. (2016), a hyperspectral imaging system with 192 spectral bands has been utilized to detect honey adulterated by sugar syrup, while in Bertelli et al. (2007), mid-infrared hyperspectral imaging with 64 spectral bands has been used to classify Italian honey. In addition, Khulal et al. (2016), Huang et al. (2013) and Li et al. (2015) have focused on assessing pork and chicken meat quality. However, the large number of spectral bands present in hyperspectral imaging resulted in difficulties in data processing, real-time implementation and longer data acquisition time. In order to overcome these limitations, different types of multispectral imaging systems have been developed with a fewer number of spectral bands which not only reduces the computational burden but improves the cost-effectiveness of the underline multispectral imaging system. However, these studies also proved that the multispectral imaging is especially suitable for adulteration detection of foods, such as detection of meat minced beef adulterated by horsemeat (Ropodi et al., 2017), detection of minced beef fraudulently substituted with pork (Ropodi et al., 2017), rapid detection of sucrose adulteration in tomato paste (Liu et al., 2017) and so on (Ennis et al., 2018; Khodabakhshian et al., 2017; Zhanget al., 2015). Most of the imaging systems mentioned above utilized complex hardware setups to obtain a large number of spectral bands and high-resolution images. Hence, these imaging systems are not viable for global commercial deployment due to high complexity and cost. Moreover, the image processing algorithms behind most of the imaging systems are primarily based on Principal Component Analysis (PCA) (Shafiee et al., 2016; Liu et al., 2017; Bandara, 2018; Bertelli et al., 2007; Khulal et al., 2016; Huang et al., 2013; Ropodi et al., 2017; Liu et al., 2017), Linear Discriminant Analysis (LDA) (Shafiee et al., 2016; Ropodi et al., 2017) and Fisher's Discriminant Analysis (FDA) (Shafiee et al., 2016) and/or Support Vector Machine (SVM) (Shafiee et al., 2016) in its raw form for dimensionality reduction, feature extraction, and regression analysis. For example, in Bertelli et al. (2007), Ropodi et al. (2017) and Liu et al. (2017), PCA has been used only in its raw to reduce the dimensions to two or three Principal Components (PCs). This kind of basic dimensionality reduction and general classification was sufficient as the underline goal of most of these work was to simply classify between contaminated and authentic.

This study involves the use of near ultra-violet (N-UV), visible and near infra-red (NIR) multispectral imaging for determining the presence of tartrazine, and rice flour in turmeric powder and then the estimation of the level of contamination. The in-house developed multi-spectral imaging system contains only nine spectral bands spanning from 375 nm to 1000 nm in the electromagnetic spectrum. A key aspect of this work is the use of this 'nine band' in-house built multispectral imaging system which only utilizes a set of off-the-shelf narrowband LEDs for the acquisition of images. Hence, the hardware setup utilized was less complex and cost-effective compared to previous proposed multispectral imaging systems, making it ideal for commercial grade use. However, as a result, the images would carry a lesser amount of spectral information and tend to be noisier compared to most imaging systems used in existing literature mentioned previously. Therefore, while high-end systems with a large number of spectral bands can rely on basic signal processing techniques such as PCA, LDA, FDA and regression modeling, etc. for simple classifications as stated previously, the proposed system uses a more cost-effective approach that puts a

greater burden on the signal processing section. Hence, the proposed methodology is multi-stage signal processing system which not only classifies but estimates the adulteration level through the development of a functional relationship. Hence, making significant enhancements on the use of signal processing for contamination level estimation in food quality analysis. The initial stages after the acquisition of the multispectral images use basic image pre-processing tools such as dark current subtraction and adaptive filtering techniques to mitigate camera sensory defects and noise impact. Thereafter, PCA was utilized as a dimension reduction step to reduce any correlated spectral information due to spectral overlap between bands. This was followed by the construction of a multivariate Gaussian distribution for each class (adulteration level) and the authentic sample. Finally, a functional relationship was obtained between the Bhattacharyya distance between each class with the pure sample class and the adulteration level. This relationship function enabled the proposed method to achieve high curve fitting ( $R^2 = 0.9911$  and SSE = 0.08451) and validation accuracy ( $R^2 = 0.9816$  and SSE = 1.1423) despite the use of low quality images. Therefore, the major contribution of the proposed work is the introduction of this robust multi-stage signal processing and classification technique which achieves high accuracy levels in the estimation of the adulteration level in low-quality MSI.

The rest of the paper is organized as follows. The Materials and Methods section presents the overview of the in-house developed multispectral imaging system, signal pre-processing steps (dark current subtraction, adaptive filtering, and PCA based dimensional reduction phase), multivariate Gaussian model construction and construction of the functional relationship between the Bhattacharyya distance and the adulteration level. Finally, the results and discussion section presents the validation and verification of the proposed method and a field test to show commercial applicability.

## 2. Materials and methods

### 2.1. Preparation of samples

Authentic turmeric (*Curcuma longa*) powder samples were prepared using fresh turmeric rhizomes collected from New Ranweli Spice Garden, Kandy, Sri Lanka. The cleaned rhizomes were sun-dried, finely ground and passed through a sieve of 300  $\mu\text{m}$  mesh to obtain powder with uniform particle size. Adulteration mixture was prepared by mixing rice flour with tartrazine (synthetic yellow azo dye, E number -

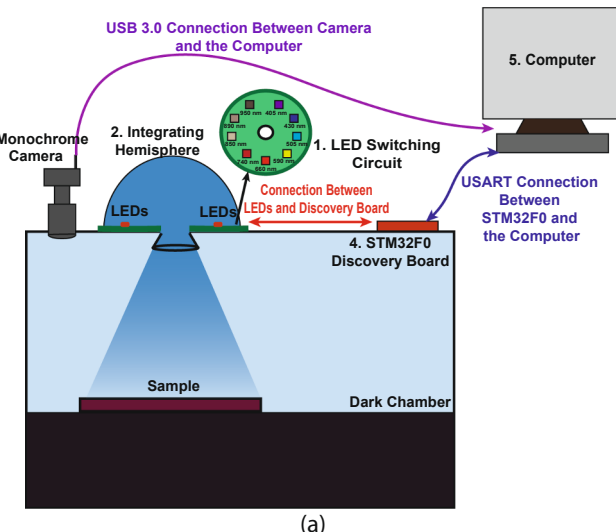


**Fig. 1.** (a) Schematic diagram of the proposed multispectral imaging system. (b) A block diagram illustrating the key steps of multispectral image acquisition.

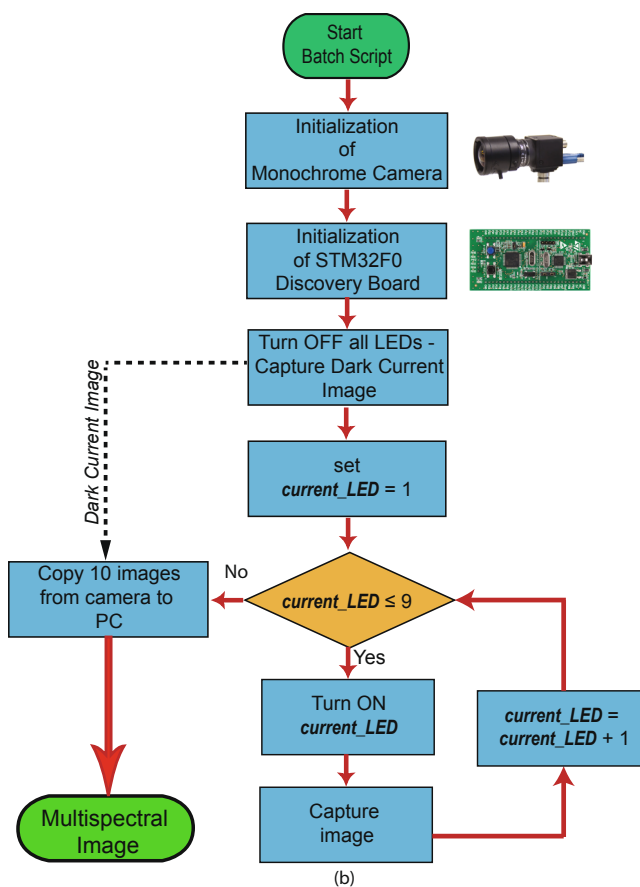


Fig. 1. (continued)

E102) at 9:1 (w/w) ratio. The authentic turmeric sample was adulterated with the prepared mixture by homogeneously mixing the adulterant at different ratios ranging from 0% to 40% (w/w). Thirty replicates were prepared for each adulteration level of 0, 5, 10, 15, 20, 25, 30, 35 and 40% (w/w). These samples (totally  $9 \times 30 = 270$  samples) were used for the purpose of calibration. At the same time, sixty more independent samples were prepared with known adulteration levels from 0 to 40% (w/w) and those samples were used for validation and verification of the proposed method. Furthermore, ten different commercially available turmeric powder samples were collected from three different geographical regions and five replicates were taken from each sample to show the commercial applicability of the proposed method. Finally, the multispectral images of the calibration samples, validation samples, and commercially available samples were captured using the developed multispectral imaging system.

## 2.2. Multispectral imaging system

A multispectral imaging system (Goelet al., 2015; Bandara et al., 2018b; Prabhath et al., 2019) was developed based on the wavelengths selected from near UV to NIR region of the electromagnetic spectrum. As shown in Fig. 1 - (a), the system consists of five components: an LED switching circuit (LEDs with peak wavelengths 405 nm, 430 nm, 505 nm, 590 nm, 660 nm, 740 nm, 850 nm, 890 nm and 950 nm), an integrating hemisphere (Radiometry, 2009)(inner diameter – 130 mm and made up of Al), a monochrome camera (FLIR Blackfly S Mono, 1.3 MP, USB3 Vision camera, Resolution – 1280 × 1024, ADC – 10 bit), a discovery board (STM32F0DISCOVERY) and a computer (Acer Aspire E 15, Intel core i5 @2.8 GHz, 8 GB DDR4 Memory). The details of the LEDs used in the LED switching circuit are given in Table 1. The emission intensities of all the LEDs were adjusted to a constant approximated value using the LED driver ICs (MAX16839ASA+). The

resulting power spectral density distribution curves of the LEDs are shown in Fig. 2.

In addition, the following criteria were taken into consideration when selecting the LED center wavelengths.

1. Most existing food quality based works have utilized wavelengths from near UV to NIR (Shafiee et al., 2016; Khulal et al., 2016; Li et al., 2015; Liu et al., 2017; Khodabakhshian et al., 2017).
2. The camera frequency response (camera is sensitive from 350 nm to 1080 nm, with peak quantum efficiency at 560 nm) coincides with the spectrum.
3. The exact positioning of the in-between LED center frequencies selected according to commercial availability as one of the primary criteria of the proposed solution is cost-effectiveness and the accessibility.

## 2.3. Multispectral image acquisition

Capturing a multispectral image requires a good synchronization between the monochrome camera and the computer. In our design, a windows batch script was developed to achieve this requirement. When the batch script was executed, a command is sent to turn ON the camera through the USB interface between the camera and the computer. When the camera is turned ON, batch script next sends a command to the discovery board to activate the first LED on the LED driver circuit through UART interface. When this signal received by the discovery board, it will immediately turn ON the first LED for about 3 s. During this short period of time, the batch script sends a command to the camera to capture the image. After the acquisition is completed by the camera, the batch script sends a command to the discovery board to turn OFF the first LED and turn ON the second LED. This procedure is repeated for all the LEDs. At the end of this process, captured images copy from the camera storage to the computer for the multispectral image analysis. A block diagram illustrating the multispectral image acquisition process of the proposed system is shown in Fig. 1 - (b).

## 2.4. Multispectral data analysis

Most of the multispectral/hyperspectral imaging systems described in the literature have mostly dealt with single-step signal processing algorithms such as PCA, LDA, FDA, SVM or regression modeling and they have the luxury of doing that due to two reasons.

1. They have used high-resolution images with a large number of spectral bands.
2. Their only requirement in all of these background works to simply classify between authentic and contaminated food.

However, the underline contribution of this paper was the construction of the functional relationship between the Bhattacharyya distance with the adulteration level which will enable us to estimate the adulteration level with high accuracy in low-quality MSI. Therefore, the proposed algorithm consists of multiple stages as shown in Fig. 3. In the first stage of the algorithm dark current subtraction and adaptive filtering were performed to mitigate camera sensory defects and random noise. Next, the samples were classified into multiple levels that are pure and contaminated turmeric samples with an increment of 5%. So any general classification problem would be simply putting the test samples into one of those adulteration levels and there is no interpolation among the classes. For us to have an interpolation among the classes we need a functional relationship. The functional relationship that we have obtained happens after the PCA step which tells us the parametric relationship between the statistical parameter (the Bhattacharyya Distance) and the adulteration level which enables us to estimate the adulteration level (not just classify). In addition to that even if those adulterated levels were separated at by a reasonable degree still it

**Table 1**

Details of the LEDs used in the LED switching circuit (Purchased from Digi-Key Electronics - <https://www.digikey.com>).

LED No.	Label	Manufacturer Part Number (Manufacturer)	Peak Wavelength (nm)	Emitting wavelength range (nm)	Linewidth (nm)
1	Near UV	VLMU3100 (Vishay)	405	375–425	10
2	Visible-Violet	<b>SM0603BWC (Bivar)</b>	430	385–525	50
3	Visible-Green	SM1204PGC (Bivar)	505	450–550	20
4	Visible-Yellow	5973209202F-ND (Dialight)	590	520–620	10
5	Visible-Orange	5975112402F (Dialight)	660	630–685	20
6	Visible-Red	QBHP684-IR4BU (QT Brightek)	740	690–760	20
7	NIR-Low	VSMY2850G (Vishay)	850	825–875	10
8	NIR-Medium	<b>VSMF4710-GS08 (Vishay)</b>	890	865–915	10
9	NIR-High	<b>VSMS3700-GS08 (Vishay)</b>	950	915 - 1000	20

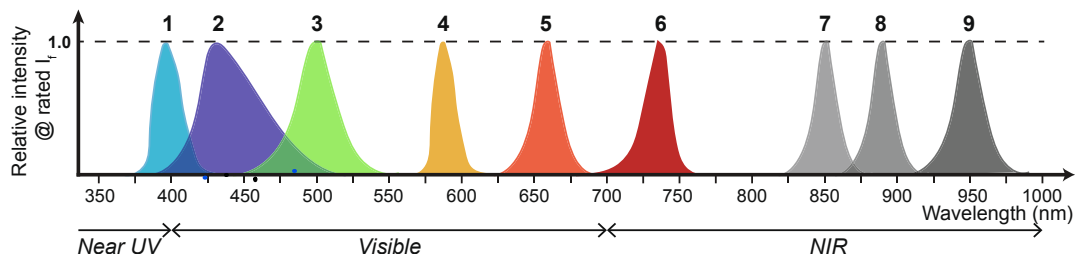


**Fig. 2.** The power spectral density distribution curves of the LEDs used in the LED switching circuit. The numbered curves from 1 to 9 correspond to the LED number shown in Table 1.

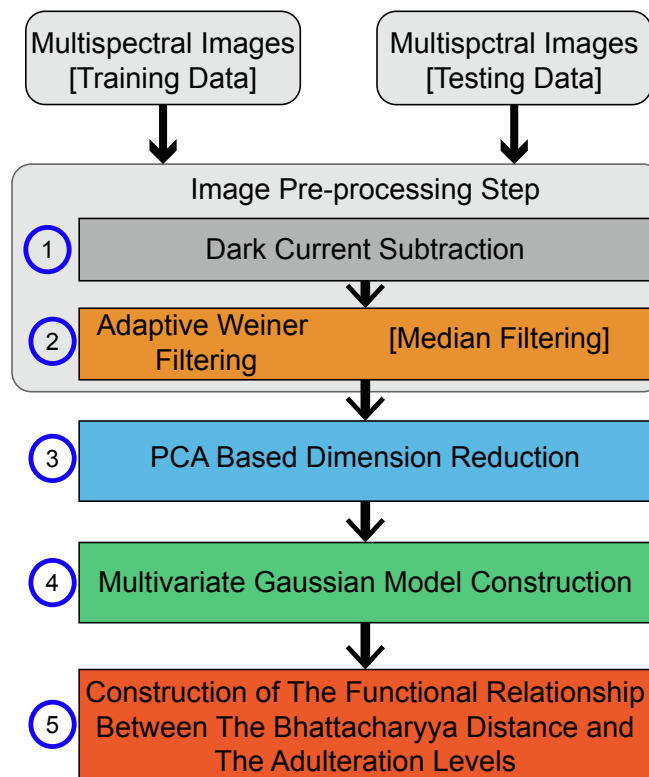


**Fig. 3.** A block diagram illustrating the proposed multi-stage signal processing algorithm to estimate the adulteration levels of turmeric powder samples. The proposed algorithm consists of five stages: dark current subtraction to mitigate camera sensory defects, adaptive filtering stage to remove random noise, PCA based dimension reduction step, multivariate Gaussian model construction step and construction of the functional relationship between the Bhattacharyya distance and the adulteration level.

doesn't provide a functional relationship.

The following sub-sections describe the underline theory behind each of these step.

#### 2.4.1. Image pre-processing

Different types of random noise including camera read-out noise, wire connection and data transfer noise between the camera and the computer, electronic noise inherent to the camera such as dark current, and noise from digitizing while converting from Analog to Digital (A/D) can result in multispectral imaging systems (Reibel et al., 2003; Hoshino et al., 2007; Yoo et al., 2007). These noise components have a definite impact on the results generated from multispectral image analysis. In the image preprocessing step, dark current subtraction and spectral low pass filtering were performed to remove random noise.

Dark current is mainly due to the currents that are generated as a result of the formation of the depletion region (York, 2011) and irregularities of the silicon lattice surface of the photodiode. This current is added to the current from drift and diffusion in the photosensor so that even if there is no external light, pixels will still measure a current. Therefore, instead of simply using sample data for the multispectral image analysis, the dark current can be subtracted from the sample data prior to any further analysis. The dark current images were taken at the beginning of each multispectral image acquisition. Then dark current subtraction was performed on each spectral image using the equation reported by (Porter et al., 2008; Sun, 2010),

$$P[\lambda] = S[\lambda] - D \quad (1)$$

where  $P[\lambda]$  is the dark current removed image at wavelength  $\lambda$ ,  $S[\lambda]$  is the raw image at wavelength  $\lambda$  and  $D$  is the dark current image captured at the beginning of the multispectral image acquisition. This will remove some inherent noise generated in the image sensor which is better than using the raw sample data as it is for the analysis.

The median filtering and 2D adaptive filtering were performed separately on the dark current subtracted image ( $P$ ) to remove random noise. The median filtering (Lim, 1990) is the simplest way of smoothing the image. The median filtering was performed by running a moving average filter on each pixel with a window size of [3 pixels  $\times$  3 pixels] using the equation given by,

$$P_{ma}^*[i, j] = \frac{1}{N} \sum_{k=-m}^{k=+m} \sum_{l=-m}^{l=+m} P[i+k, j+l] \quad (2)$$

where  $P_{ma}^*$  is the filtered image after the moving average filtering,  $P$  is the dark current subtracted image,  $m = 1$ ,  $N = (2m + 1)^2 = 9$  is the

total number of pixels in the selected window and  $P[i + k, j + l]$  represents the intensity value of the pixel located at  $(i + k)^{th}$  column and  $(j + l)^{th}$  row of the dark current subtracted image ( $P$ ).

At the same time, an adaptive Wiener filter was also tested to remove random noise in the dark current subtracted image ( $P$ ) and the performance was compared with results obtained for median filtering. The main difference in adaptive Wiener filtering compared to the median filtering is that filter parameter are space variant. In other words, filter coefficients (pixel mean -  $\mu[i, j]$  and variance -  $\sigma^2[i, j]$ ) change as a function of  $[i, j]$ . Therefore, the pixel mean ( $\mu[i, j]$ ) and the variance ( $\sigma^2[i, j]$ ) are not fixed for the entire image and they are calculated locally at each pixel location. The local mean ( $\mu[i, j]$ ) at the pixel location  $[i, j]$  can be calculated using the equation given by,

$$\mu[i, j] = \frac{1}{N} \sum_{k=-m}^{k=+m} \sum_{l=-m}^{l=+m} P[i + k, j + l] \quad (3)$$

where  $P$  is the dark current subtracted image and  $N (= (2m + 1)^2 = 9)$  is the total number of pixels in the selected window. The local variance ( $\sigma^2[i, j]$ ) at the pixel location  $[i, j]$  can be evaluated using the equation given by,

$$\sigma^2[i, j] = \left( \frac{1}{N^2} \sum_{k=-m}^{k=+m} \sum_{l=-m}^{l=+m} P^2[i + k, j + l] \right) - \mu^2[i, j] \quad (4)$$

The white noise variance ( $v^2$ ) is assumed to be constant over the entire image and can be calculated by averaging all the locally estimated variances ( $\sigma^2[i, j]$ ) using the equation given by,

$$v^2 = \frac{1}{L \times W} \sum_{i=0}^{i=L} \sum_{j=0}^{j=W} \sigma^2[i, j] \quad (5)$$

where  $L$  is the length of the multispectral image (No. of pixels),  $W$  is the width of the multispectral image (No. of pixels) and  $L \times W$  is the total number of pixels in the image. Finally, the Wiener filtered image ( $P_w^*$ ) can be obtained using the equation given by (Lim, 1990),

$$P_w^*[i, j] = \mu[i, j] + \frac{\sigma^2[i, j] - v^2}{\sigma^2[i, j]} (P[i, j] - \mu[i, j]) \quad (6)$$

It is worthwhile to mention the rationale behind the selection of the particular window size of [3 pixels  $\times$  3 pixels]. The primary operation of the adaptive Weiner filtering or median filtering is noise mitigation. Hence, its underline operation could be a low pass smoothing operation. However, if it is done extensively as the adulterants themselves act as high-frequency fluctuations there would be a danger of the removal of actual information. Therefore, the appropriate lowest order ( $m = 1$ ) which would optimally make the compromise was selected. When higher orders were used (i.e.  $m = 2, 3, 4, \dots$ ) as mentioned it was observed that in addition to noise removal certain fluctuations pertaining to adulterant information was removed. In other words, there is a fine line between the high-frequency noise and high-frequency information. Hence, the filter order was selected in such a way that noise is mitigated while the useful adulterant specific information was kept. For example, when examining higher order cases of the Weiner filter and median filter realizations it was noticed that most of the adulterants information was removed.

#### 2.4.2. Spectral signatures

An example multispectral image of turmeric which was obtained after the image pre-processing step is shown in Fig. 4 – (a). A random pixel (red dot) was selected in the region of turmeric powder and the grayscale values (between 0 and 255) were plotted against the wavelength to obtain the spectral signature as shown in Fig. 4 – (b).

In the next step, data-matrixes belonging to each adulteration level were created from the multispectral images. As mentioned previously, for each adulteration level (let's denote as  $p\%$  (w/w) and  $p = 0, 5, 10, 15, \dots, 40$ ) thirty replicates were prepared. Hence, when creating the

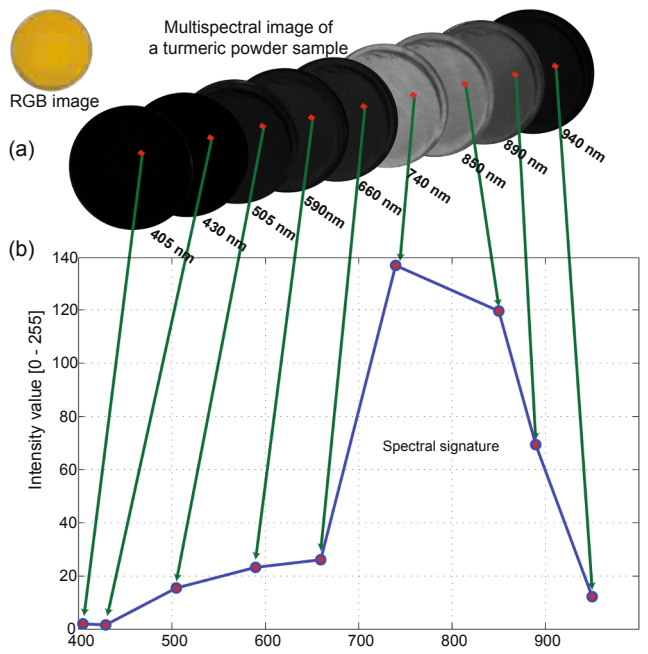


Fig. 4. (a) A multispectral image of a turmeric powder sample captured from the in-house developed multispectral imaging system (b) The spectral signature (variation of the pixel intensity value with wavelength) of the selected pixel (marked in red color).

data-matrix which corresponding to each adulteration level, 100 pixels were randomly selected from the multispectral image for each replicate for that particular adulteration level. As shown in Fig. 5, each data matrix has 9 columns ( $n$ ) to represent the spectral intensities of the nine spectral bands and 3000 rows ( $m$ ) as there were altogether 3000 pixels for each adulteration level (100 pixels for each of the 30 replicate for each level). Therefore, the data matrix corresponding to  $p\%$  (w/w) adulterated turmeric can be denoted as  $X_p(m, n)$  where,  $p$  goes from 0 to 40% at 5% increments, where  $m = 3000$  and  $n = 9$ .

When the data matrixes for all the adulteration levels ( $X_p(m, n)$ , for  $p = 0, 5, 10 \dots 40$ ) were created, mean spectral intensity values along the nine dimensions (9 spectral bands) were calculated and denoted as  $\bar{X}_p$  as shown in Fig. 5. Thus, the dimensions of the  $\bar{X}_p$  is  $1 \times 9$ . Next, the variation of the average spectral intensity values with the wavelength for different adulteration levels were shown in Fig. 6 however, they are not noticeably distinguished. Therefore, the identification of adulterated turmeric by the mean spectral signatures is not a viable solution, as it can lead to incorrect results. In order to reduce the data redundancy and to improve the discrimination between classes (adulterated levels), PCA was performed on the nine-dimensional dataset. In addition, it would allow us to reduce the correlation between each spectral band and pave the way to the construction of the functional relationship between a statistical metric and the adulteration level in a more efficient manner.

#### 2.4.3. Principal Component Analysis (PCA)

Because of the overlap between several adjacent spectral bands, as shown in Fig. 2, the nine bands of spectral information that we were extracted from the imaging system is not fully uncorrelated. Therefore, the PCA step was carried out in its traditional scenes to do a simplified dimension reduction which will enable us to construct the multivariate Gaussian distribution function in a more efficient manner.

Initially, the data matrix –  $X$  was formulated with  $q$  number of rows and  $n$  number of columns. Here, the number of columns ( $n$ ) corresponds to the nine spectral bands and the number of rows ( $q$ ) equal to the total number of pixels selected from each multispectral image of training data. Therefore, entries in the data matrix –  $X$  can be written as,

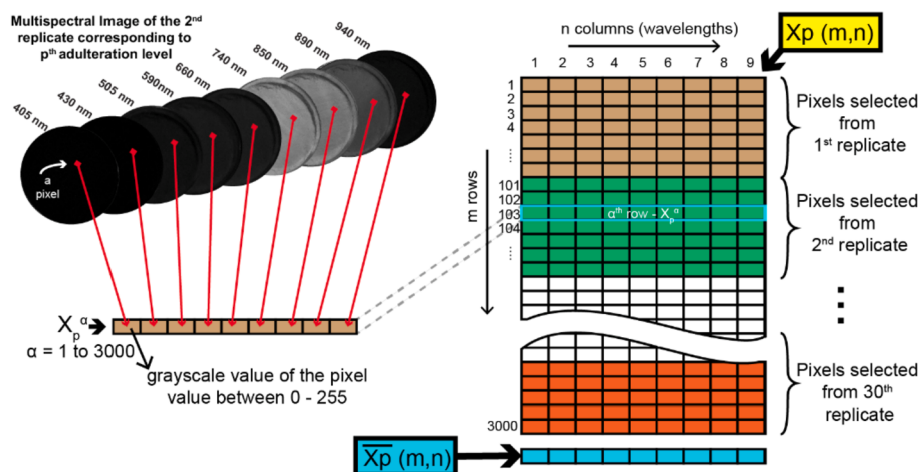


**Fig. 5.** The extraction of multispectral image data to create data-matrix ( $X_p$ ) corresponding to  $p\%(\text{w/w})$  adulterated turmeric powder where  $p = 0, 5, 10, \dots, 40$ .

$$X = [X_0, X_5, X_{10}, X_{15}, X_{20}, X_{25}, X_{30}, X_{35}, X_{40}]^T$$

where,  $X_0, X_5, X_{10}, \dots$ , and  $X_{40}$  represent the data matrixes corresponding to adulteration levels of 0%, 5%, 10%, ..., and 40% respectively. As described in the previous section, each of these  $X_0, X_5, X_{10}, \dots$ , and  $X_{40}$  contain spectral information of 3000 data points selected from 30 replicates (dimensions of  $X_p = m \times n = 3000 \times 9$ ). Thus the dimensions of the data matrix- $X$  is  $q \times n$ , which is equal to  $27,000((9m) \times 9)$ . After that PCA was performed on the data matrix -  $X$  as given in [Zabalzaet al. \(2014\)](#), [Manolakis et al. \(2016\)](#), and [Vithana et al. \(2018\)](#). The basic steps of the PCA algorithm can be summarized as follows:

- Step 1: Calculation of mean vector ( $\mu$ ) - the vector which represents the mean spectral information (intensities) of the pixels (dimensions =  $9 \times 1$ ):

$$\mu = \frac{1}{m} \sum_{\alpha=1}^m (X^\alpha)^T$$

where,  $X^\alpha$  (dimensions =  $9 \times 1$ ) is the vector representing the spectral information of a pixel (in other words,  $\alpha^{\text{th}}$  row of the data matrix -  $X$ ).

- Step 2: Calculating the covariance matrix -  $C$  (dimensions =  $9 \times 9$ ):

$$C = \frac{1}{m} \sum_{\alpha=1}^m (X^\alpha - \mu)(X^\alpha - \mu)^T$$

where,  $T$  represents the matrix transpose.

- Step 3: calculation of eigenvalues ( $\lambda_k$ ) and corresponding eigenvectors ( $v_k$ ) of the covariance matrix ( $C$ )

$$Cv_i = \lambda_i v_i; \text{ for } i = 1, 2, 3, \dots, 9$$

where,  $\lambda_1 \geq \lambda_2 \geq \dots \geq \lambda_k \geq \dots \geq \lambda_9$ .

- Step 4: Extraction of principal components (PCs) corresponding to high valued  $\lambda_k$ ,

$$P = [v_1, v_2, v_3, \dots, v_k] \text{ and } k \leq 9$$

where,  $v_k$  is the  $k^{\text{th}}$  eigenvector corresponding to  $k^{\text{th}}$  largest eigenvalue and  $P$  is denoted as transformation matrix. The value of the  $k$  was selected such that it captures 95% of the total variance as shown in [Fig. 7 – \(a\)](#) (in our case the value of  $k = 6$ ). Therefore, the dimensions of the matrix  $P$  is  $9 \times 6$ .

- Step 5: Projection of raw data matrix -  $X$  into the reduced PC subspace,

$$Y = XP$$

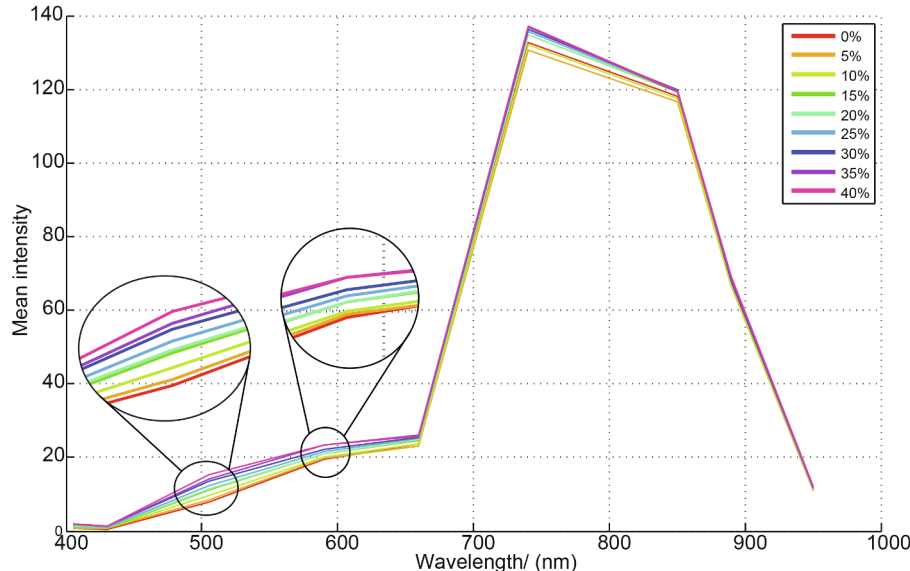


**Fig. 6.** Mean spectral signatures for different adulteration levels ranging from 0% to 40% at 5% increments.

where,  $Y$  is the matrix representation of  $X$  in the reduced dimensional space. The dimensions of the  $Y$  is  $(27000 \times 6)$ .

Most existing algorithms have utilized PCA as the final stage of their signal processing algorithm. Fig. 7 – (b) demonstrates the cluster formation when the algorithm was stopped at the PCA stage. As can be seen from Fig. 7 – (b), the PCA result clearly shows the demarcation between the authentic turmeric class and the adulterated turmeric classes. However, the adulterated turmeric classes show significant cluster overlap in the PC<sub>1</sub>-PC<sub>2</sub> space. Further, it was observed that when taking higher-numbered PC pairs (i.e. PC<sub>1</sub>-PC<sub>3</sub>, PC<sub>1</sub>-PC<sub>4</sub>, PC<sub>1</sub>-PC<sub>5</sub>, PC<sub>2</sub>-PC<sub>3</sub>, PC<sub>2</sub>-PC<sub>4</sub>, ..., etc.), it led to even more overlap between different levels of adulterated turmeric classes as well as at times an overlap with the authentic turmeric class itself. This is in tally with the basic premise of PCA, where the higher-valued (lower variance) PCs would correspond to the directions which have higher noise content. Therefore, PCA result do not provide any feasible information that can be used to effectively develop a functional relationship between the adulteration levels. Hence the Gaussian model construction and Bhattacharyya distance stages are required to achieve these requirements.

The multivariate Gaussian distributions with  $k$  dimensional mean ( $\mu_p^{\text{reduced}}$ ) vector and  $k \times k$  covariance matrix ( $C_p^{\text{reduced}}$ ) were obtained from the PCA result which will act as a primary descriptor for each of the nine adulteration levels. Therefore, leading to the next stage of this algorithm, our aim is to quantify the distance between these multivariate Gaussian structures given by the Bhattacharyya distance to better emulate the relationship between the adulteration levels.

#### 2.4.4. Bhattacharyya distance and Jeffries-Matusita (JM) separability measure

In order to establish a functional relationship with the adulteration level, Jeffries-Matusita (JM) distance was utilized. JM distance measures the separability (distance) between two multivariate Gaussian distributions. It was observed that the spectral intensity values correspond to each adulteration level in the reduced PC space ( $PC_1, PC_2, \dots, PC_k$ ) forms approximately Gaussian distributions along each principal component axis. Therefore, it can be assumed that the probability distribution functions corresponding to each adulteration level are multivariate Gaussian distributed. With this assumption, the dissimilarity between each class ( $Y_p^{\text{reduced}}$ ) and pure turmeric class ( $Y_0^{\text{reduced}}$ ) can be measured using the Jeffries-Matusita (JM) distance  $J(f_{Y_0}, f_{Y_p})$  (Ahmad and Quegan, 2012; Richards and Jia, 1999) given by,

$$J(f_{X_0}, f_{X_p}) = \sqrt{2(1 - e^{-B(f_{Y_0}, f_{Y_p})})} \quad (7)$$

$$\begin{aligned} B(f_{Y_0}, f_{Y_p}) = & \frac{1}{8}(\mu_0^{\text{reduced}} - \mu_p^{\text{reduced}})^T \left[ \frac{C_0^{\text{reduced}} + C_p^{\text{reduced}}}{2} \right]^{-1} (\mu_0^{\text{reduced}} - \mu_p^{\text{reduced}}) \\ & + \frac{1}{2} \ln \left( \frac{|C_0^{\text{reduced}} + C_p^{\text{reduced}}|}{\sqrt{|C_0^{\text{reduced}}||C_p^{\text{reduced}}|}} \right) \end{aligned} \quad (8)$$

where,  $J(f_{Y_0}, f_{Y_p})$  is the Jeffries-Matusita (JM) separability measure between the two multivariate Gaussian distribution functions  $f_{Y_0}$  and  $f_{Y_p}$ ,  $B(f_{Y_0}, f_{Y_j})$  is the Bhattacharyya distance between the two Gaussian distribution functions  $f_{Y_0}$  and  $f_{Y_p}$ ,  $\mu_p^{\text{reduced}}$  ( $n \times 1$ ),  $\mu_0^{\text{reduced}}$  ( $n \times 1$ ) are the mean vectors and  $C_0^{\text{reduced}}$  ( $n \times n$ ),  $C_p^{\text{reduced}}$  ( $n \times n$ ) are the covariance matrixes in the reduced PC space. The range of  $J(f_{Y_0}, f_{Y_j})$  is from 0 to 2. When a turmeric powder sample contains adulterants, its multivariate distribution function ( $f_{Y_p}$ ) differs from the authentic turmeric ( $f_{Y_0}$ ). The degree of dissimilarity between the two distributions depends on the adulteration level. Therefore, from the mathematical point of view, when more and more adulterants were mixed with authentic turmeric powder, its multivariate distribution function differs more and more from the pure turmeric and as a result, the distance between two classes increase significantly. According to the value of  $J(f_{Y_0}, f_{Y_j})$ , it is possible to categorize the quality of turmeric powder samples into three regions:

$$J(f_{Y_0}, f_{Y_j}) = \begin{cases} 2.0 \geq J > 0.9 & \text{Grade C: Highly adulterated turmeric} \\ 0.9 \geq J > 0.5 & \text{Grade B: Moderately adulterated turmeric} \\ 0.5 \geq J > 0 & \text{Grade A: Very close to authentic turmeric} \end{cases}$$

In detail, if a turmeric powder sample falls into Grade A, that means its properties are more identical to the authentic turmeric powder (adulteration level < 5%), if a turmeric powder sample falls into Grade B that means it is moderately adulterated (5% < adulteration level < 15%) and if a turmeric powder sample falls into Grade C that means the sample is highly adulterated (adulteration level > 15%).

#### 2.5. Microscopic analysis

As mentioned earlier, a field test was conducted to demonstrate the commercial applicability of the proposed algorithm in addition to the proper performance evaluation step described in Section 3.3. For the field testing, ten commercially available samples were taken from different geographical regions of Sri Lanka. Then, the adulteration levels of each commercial sample were estimated using the proposed algorithm and the results were verified from a microscopic analysis. It is worthwhile to mention that, there is no highly precise single technique to determine the exact adulteration percentage of turmeric powder by physical and chemical methods. Therefore, the research team decided to observe each commercially available sample under a light microscope to differentiate authentic and contaminated commercial turmeric samples, which would be accurate enough for the field testing as the proper performance validation was carried out with exactly known adulteration levels in section 3.3.

In the microscopic analysis (Bouzabata, 2019), small quantities from each commercially available sample were primarily observed under OBE 108 transmitted light microscope. The powdered sample was spread evenly on a microscope slide with the help of little amount of distilled water. The mixture was covered with a coverslip, and excess water was removed by blotting the edges of coverslip gently with a filter paper. Observations were taken under the middle ( $10 \times 10 = 100$ ) and maximum power ( $10 \times 40 = 400$ ) of the objective lens. Furthermore, the turmeric samples were examined under the microscope using iodine and sodium hydroxide solutions for the

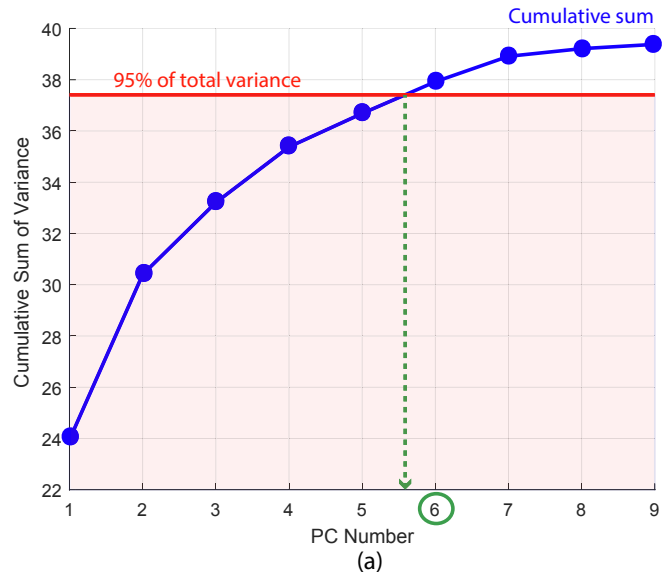


Fig. 7. (a) The cumulative sum of PCs which are ranked in descending order of the amount of variance. The number of principal components used in reduced PC subspace ( $k$ ) was selected such that it captures at least 95% of the total variance. (b) Scores plot of PC1 Vs. PC2 from PCA for different adulteration levels of training samples. The figure shows significant cluster overlap for adulterated turmeric.

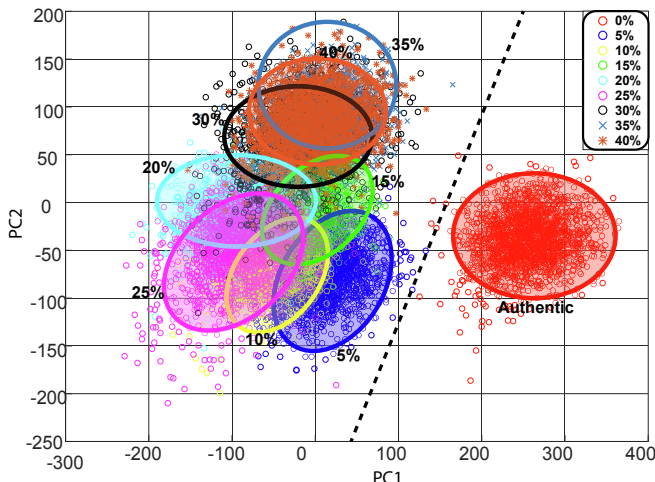


Fig. 7. (continued)

identification of starch granules and turmeric particles respectively. The compulsory micrographs of each commercially available sample were shown in Fig. 12 in order to support the field test results given in Table 2 in section 3.4.

### 3. Results and discussion

#### 3.1. Selection of the optimal filter and filter parameters

To remove the random noise present in multispectral images two types of filtering methods were tested separately at the image pre-processing step: the median filtering and the Wiener filtering. The best filter type and the window size ( $n$  pixels  $\times$   $n$  pixels) were determined such that it maximizes the coefficient of determination ( $R^2$ ) for the curve fitting results. If the size of the window is too large, the filter blurs the image and sometimes it results in the disappearance of the useful

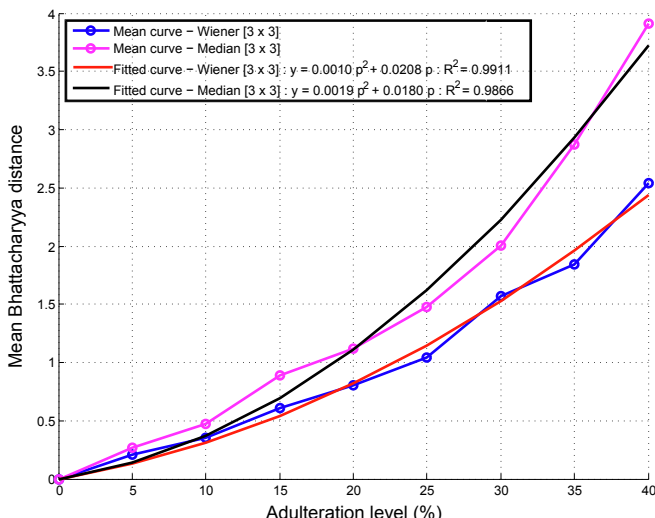


Fig. 8. The curve fitted results for variation of Bhattacharyya distance with the adulteration level under two different filtering methods: median filtering and adaptive Wiener filtering with a window size of [3 pixels  $\times$  3 pixels]. Maximum  $R^2$  (0.9911) and minimum SSE (0.08451) values were obtained for the adaptive Wiener filtering.

information present in the multispectral image. On the other hand, if the window size is too small, random noise will still be present in the image. Therefore, a reasonable window size (3 pixels  $\times$  3 pixels) was selected. For the (3 pixels  $\times$  3 pixels) window size, the median filtering resulted in an  $R^2$  value of 0.9866 and the Wiener filtering resulted in an  $R^2$  value of 0.9911 as shown in Fig. 8. The performance of the curve fitting results under these two different filtering methods are summarized in Table 2. Finally, the adaptive Wiener filtering with the window size of (3 pixels  $\times$  3 pixels) was performed at the image pre-processing step following the dark current subtraction.

#### 3.2. Estimation of adulteration level

The purpose of the training phase is to establish a functional relationship between the statistical metric (i.e. the Bhattacharya Distance and the JM Distance) and the adulteration levels. That was done by utilizing the training samples at 5% (w/w) increment of the adulteration levels, where for each adulteration level 30 replicates were utilized. As can be seen from Fig. 9, the mean of the thirty samples per each adulteration level was utilized to generate the functional relationship between the adulteration level given by  $B = 0.001007 p^2 + 0.02077p + 0$  with  $R^2 = 0.9911$  and SSE of 0.08451. Also, the variation of the JM distance with the adulteration level was modeled using the equation given in (13) as shown in the same figure.

#### 3.3. Validation and verification of the proposed method

The proposed algorithm which utilizes the Bhattacharyya distance and the JM distance for the adulteration level estimation has been validated using turmeric samples whose contamination levels were pre-estimated through controlled experiment mentioned in section 2.1. As can be noted there, the ground truth that was established for that method is precisely known as the contamination was done by the research group with precisely measured quantities. Hence, as can be seen from the results presented later, the goal to accurately estimate the adulteration level of the test samples from the proposed method was successful as the estimated levels were extremely close to the well-established ground truth. The sixty samples with known adulteration levels varying from 0% to 40% (w/w) were used as the ground truth. Next, the adulteration levels of each sample were estimated from the proposed method and plotted on the calibrated model as shown in Fig. 10. It can be clearly noticed that the estimated adulteration levels came very close to the calibrated model with  $R^2 = 0.9816$  and SSE = 1.1423. It is interesting to note that, in addition to the test samples at 5% increments, even samples at intermediate levels of contamination were properly identified through the interpolative technique which was developed by constructing a fully functional relationship between the Bhattacharyya distance and the adulteration level.

#### 3.4. Field testing

Further to the performance evaluation step conducted above, the proposed algorithm was tested on commercially available products to ascertain its commercial viability in the real world. To the best of our knowledge, there is no highly precise single technique to deduce the exact adulteration level as this contamination was done in a process not privy to the research team. Therefore, the research team decided to perform a microscopic analysis of the samples. This was conducted by trained personnel and was of sufficient accuracy for the purpose of commercial applicability testing. The tests used in the study are

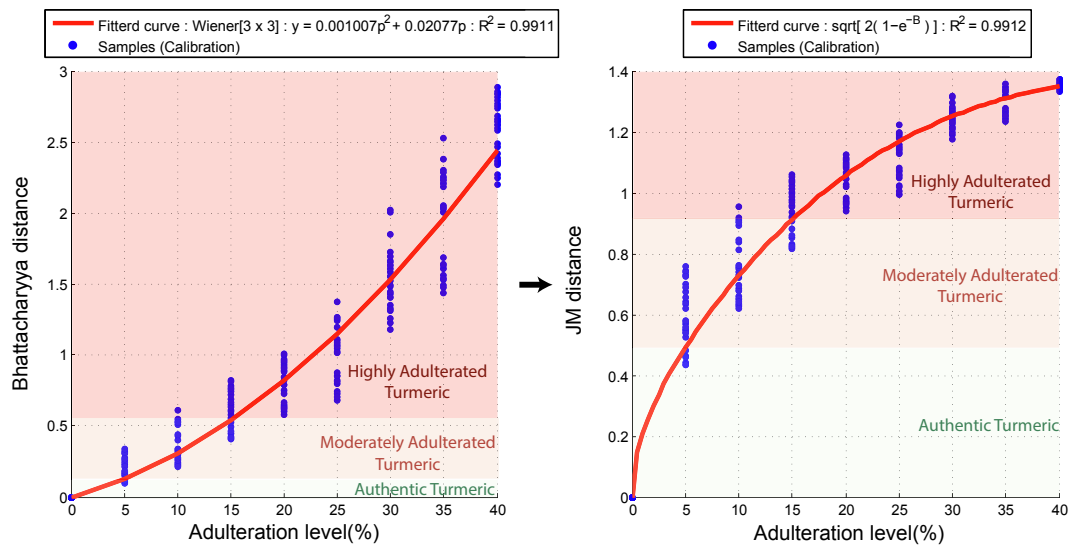


**Fig. 9.** (a) The variation of the mean Bhattacharyya distance with the adulteration level (b) The variation of the mean JM distance with the adulteration level for training data.

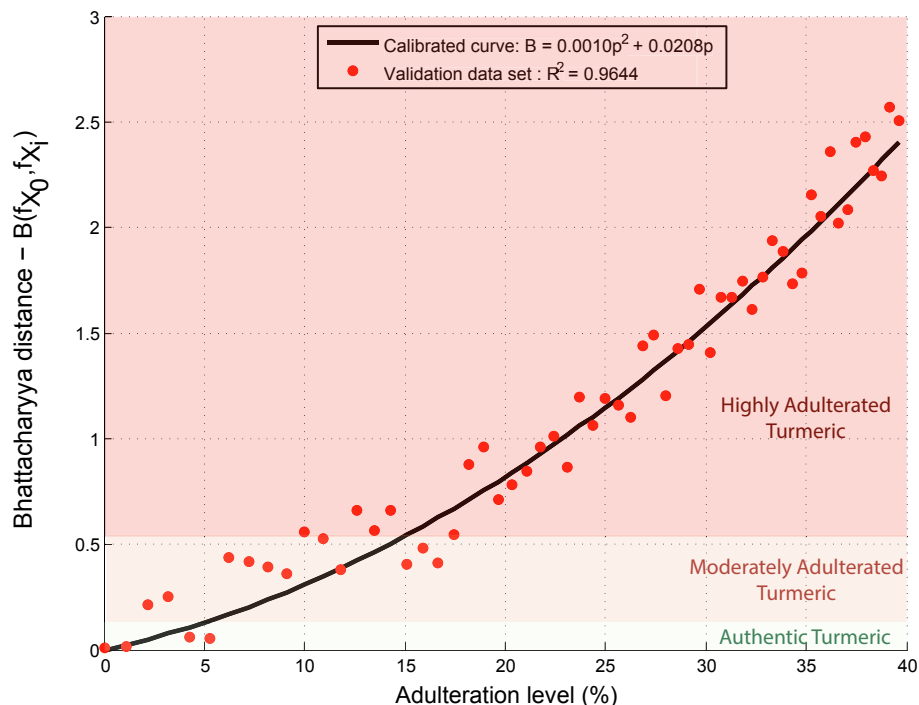


**Fig. 10.** Validation and verification of the proposed algorithm: Bhattacharyya distance between each testing sample and the authentic turmeric against their actual adulteration level (red dots). All testing samples closely follow the functional relationship ( $B = 0.001007 p^2 + 0.02077p + 0$ ) with  $R^2 = 0.9816$  and SSE = 1.1423.

commonly performed in the laboratories that are regularly used for food quality analysis in the country.

The microscopic test mentioned below was done on the commercially available products and the results were represented in Fig. 11, even though the performance of the system with algorithms has been well proved in section 3.3, the aim of this section is to show the importance of this work in a real-world commercial context.

For the field testing, the adulteration levels of ten different

commercially available products (selected from different geographical regions of Sri Lanka) were determined using the calibrated model and the results were verified from laboratory tests (microscopic analysis, NaOH test, and iodine test). These ten commercially available products were coded as CS<sub>1</sub>, CS<sub>2</sub>, CS<sub>3</sub>, CS<sub>4</sub>, CS<sub>5</sub>, CS<sub>6</sub>, CS<sub>7</sub>, CS<sub>9</sub> and CS<sub>10</sub> for easy identification. Due to the randomness that occurs in the particle placement of the mixing process, multiple realizations were analyzed for each commercial sample to ensure the repeatability of the results.

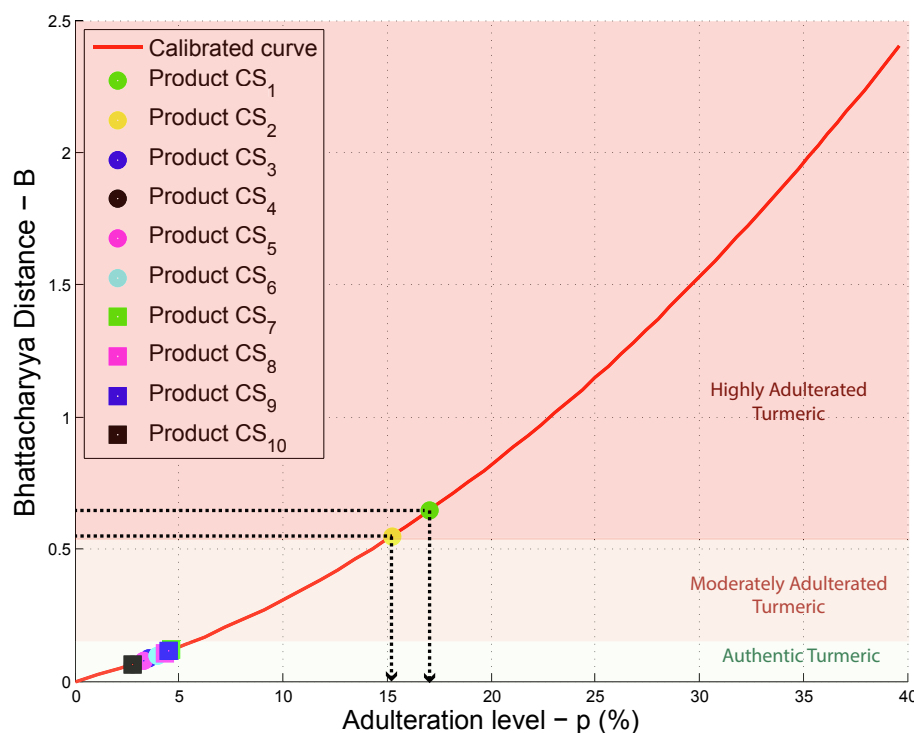


Fig. 11. Adulteration level estimation of commercial samples from the functional relationship between Bhattacharyya distance and the adulteration level.

Therefore, five replicates were taken from each commercial product that would enable us to observe the connectivity between the microscopic images and multispectral information. The Bhattacharyya distances were calculated for each replicate and mean Bhattacharyya distance was used to estimate the adulteration level of each of the sample as shown in Table 3 and Fig. 10. According to our calculations, product CS<sub>1</sub> contained adulterants with approximately 17% (w/w), product CS<sub>2</sub> contained adulterants with approximately 15%, and Products CS<sub>3</sub>, CS<sub>4</sub> CS<sub>5</sub>, CS<sub>6</sub>, CS<sub>7</sub>, CS<sub>8</sub>, CS<sub>9</sub>, and CS<sub>10</sub> contained adulterants with less than 5% (w/w). To validate the result, a small quantity from each product was analyzed using a light microscope. The micrographs of turmeric obtained under the magnification 10 × 10 are shown in Fig. 12.

As shown in Fig. 12 - (c)-1, the sample CS<sub>1</sub> contained large particles compared to authentic turmeric powder particles. The large particles were identified as adulterants by carefully observing the microscopic views of the sample CS<sub>1</sub> as NaOH was added. The color of turmeric powder particles changes to dark red when NaOH was added and extraneous particles remained unstained as shown in Fig. 12 - (c)-2. Further, the adulterants were identified as rice particles from an iodine test. Even though it is impossible to identify the exact adulteration level of turmeric powder samples using the NaOH and iodine tests, it can be used to prove that at least sample CS<sub>1</sub> contained rice particles with significant adulteration level. Our analysis estimated that sample CS<sub>2</sub> contained adulterants about 15.2%. From the microscopic view of sample CS<sub>2</sub> shown in Fig. 12 (d)-1, it can be observed that it does not contain any large particles as in the case of sample CS<sub>1</sub>. In order to identify whether sample CS<sub>2</sub> is adulterated or not, NaOH was added to a small portion of the sample CS<sub>2</sub> and was observed under the microscope. The result is shown in Fig. 12 (d)-2. From the microscopic view (Fig. 12 (d)-2) it can be clearly seen that the sample CS<sub>2</sub> contained some fine particles which are not turmeric. Therefore, it was validated that

sample CS<sub>2</sub> is adulterated. An interesting observation was made for the sample CS<sub>3</sub>. The sample CS<sub>3</sub> was identified as adulterated at its first glance under the physical and visual inspection whereas not in the multispectral identification process. However, by conducting subsequent NaOH addition and microscopic analysis with magnification 10 × 40 it was validated that sample CS<sub>3</sub> was not adulterated as shown in Fig. 12 (e)-2. All the other samples were identified as closer to authentic turmeric from the NaOH test and the iodine test. The microscopic views of samples CS<sub>4</sub> to CS<sub>10</sub> are shown in Fig. 12 - (f)-(l) respectively.

The field testing showed that there are commercially available turmeric products that are adulterated and the developed system is capable of identifying such products. Further, this proves the viability of the proposed system and the algorithm in an industrial scale application.

#### 4. Conclusion

This work outlines a novel multi-stage signal processing algorithm to estimate the contamination level of turmeric utilizing the in-house developed “nine-band” multispectral imaging system. The multispectral imaging system only uses nine narrow-band off-the-shelf LEDs with emitting wavelengths ranging from 475 nm to 1000 nm. Thus, the hardware setup is less complex, cost-effective and ideally suited for the global commercial deployment. However, fewer number of spectral bands and the low resolution of multispectral images lead to more burden on image processing algorithms. Therefore, the proposed algorithm consists of five stages; dark current subtraction and adaptive Weiner filtering stage to mitigate camera sensory defects and random noise, PCA based dimension reduction step, multivariate Gaussian model construction and finally the construction of the functional relationship between the Bhattacharyya distance and the adulteration levels. This five-stage process was able to achieve higher curve fitting

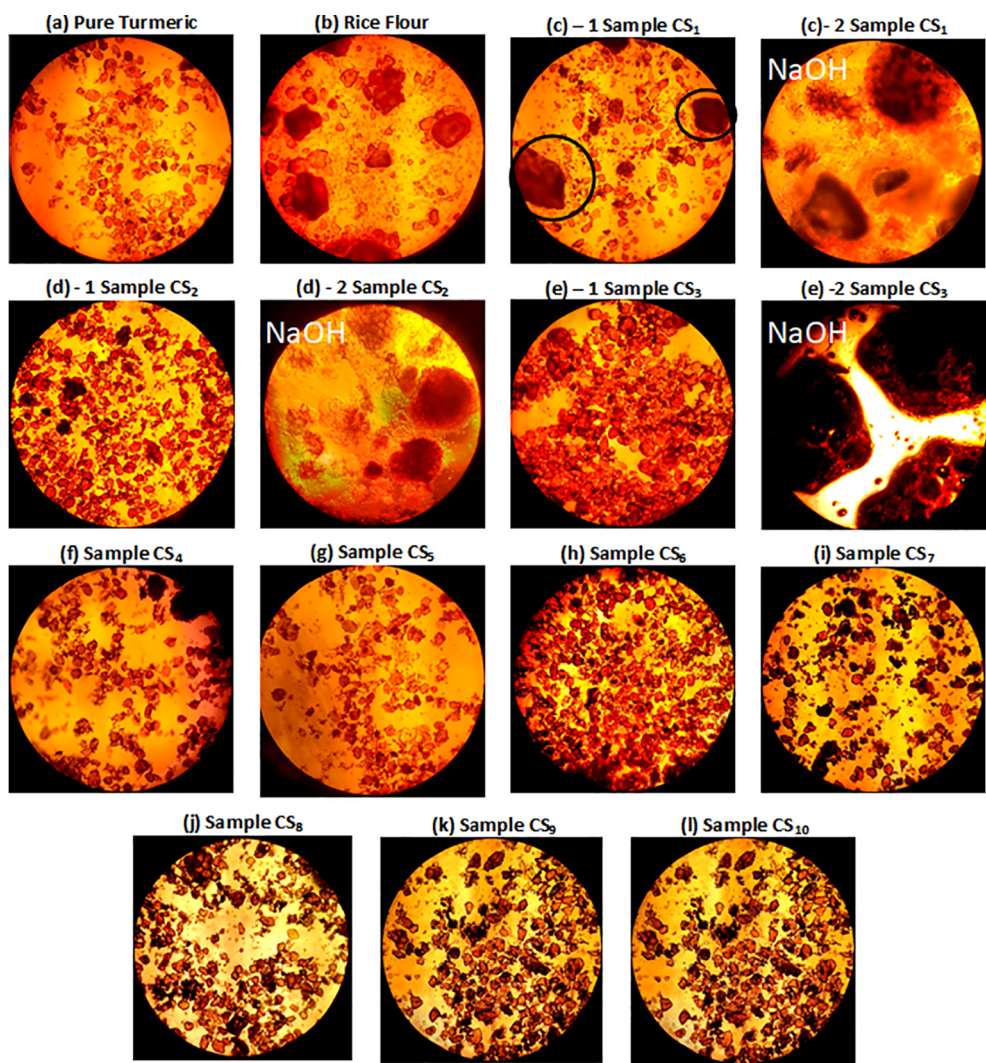


**Fig. 12.** Micrographs of (a) authentic turmeric (magnification:  $10 \times 10$ ), (b) rice flour (magnification:  $10 \times 10$ ), (c) –1 sample CS<sub>1</sub> (magnification:  $10 \times 10$ ), (c)–2 sample CS<sub>1</sub> when NaOH was added, (d)–1 sample CS<sub>2</sub> (d) –2 sample CS<sub>2</sub> when NaOH was added (magnification:  $10 \times 10$ ), (e)–1 sample CS<sub>3</sub>(magnification:  $10 \times 10$ ), (e)–2 sample CS<sub>3</sub> when NaOH was added (magnification  $10 \times 40$ ), (f)–(l) samples CS<sub>4</sub>, CS<sub>5</sub>, CS<sub>6</sub>, CS<sub>8</sub>, CS<sub>9</sub> and CS<sub>10</sub> (magnification:  $10 \times 10$ ).

**Table 2**

The performance of curve fitting results under the Wiener filtering (window size: 3 pixels  $\times$  3 pixels) and the median filtering (window size: 3 pixels  $\times$  3 pixels).

Curve fitting result:  $B = p_1p^2 + p_2p + p_3$  and  $p_3$  fixed at zero.

	Squared Error of prediction (SSE)	The coefficient of determination ( $R^2$ )	Root Mean Square Error (RMSE)	Coefficients of the polynomial	
				$p_1$	$p_2$
The Wiener filter: [3 pixels $\times$ 3 pixels]	0.0500	0.9911	0.08451	0.001007	0.02077
The median filter: [3 pixels $\times$ 3 pixels]	0.1772	0.9866	0.15910	0.001876	0.01801

results ( $R^2 = 0.9911$  and SSE = 0.08451) at the training stage.

Above all, the proposed multi-stage algorithm has been validated using an independent set of samples where contamination levels of all the samples were precisely known. Despite the use of a few spectral bands and low-resolution images, higher validation accuracy ( $R^2 = 0.9816$  and SSE = 1.1423) has been achieved due to the multi-stage nature of the algorithm. In addition to the proper validation and verification step, a field test was carried out to show the commercial applicability. For that, the adulteration levels of ten different commercial turmeric samples were estimated using the proposed algorithm

and the results were verified from laboratory tests. The results reveal that the multispectral imaging system and multi-stage algorithm works well with commercial samples and ideally suited for the commercial grade use.

Even though this study was limited to tartrazine colored rice flour as the adulterants, depending on the requirements, the algorithm can be simply modified such that it enables distinguishing between the more adulterants. This can be achievable by using a reasonable set of training samples of each adulterant.

**Table 3**

Details of estimated adulteration levels of commercially available samples.

Commercial product	Bhattacharyya distance - B					Mean Bhattacharyya distance - B	Variance	Standard Deviation	Predicted adulteration level (p)
	Replicate 1	Replicate 2	Replicate 3	Replicate 4	Replicate 5				
CS <sub>1</sub>	0.6300	0.6407	0.6743	0.6662	0.6160	0.6454	0.00060	0.0244	17.0%
CS <sub>2</sub>	0.5723	0.5503	0.5734	0.5264	0.5264	0.5497	0.00054	0.0232	15.2%
CS <sub>3</sub>	0.0765	0.1236	0.0786	0.0742	0.0797	0.0865	0.00043	0.0209	3.6%
CS <sub>4</sub>	0.0682	0.0623	0.0643	0.0720	0.0602	0.0654	0.00002	0.0047	2.8%
CS <sub>5</sub>	0.0797	0.0795	0.0790	0.0786	0.0767	0.0787	0.00000	0.0011	3.2%
CS <sub>6</sub>	0.0969	0.0991	0.0872	0.1027	0.1027	0.0977	0.00004	0.0064	3.9%
CS <sub>7</sub>	0.1127	0.1248	0.1190	0.1163	0.1163	0.1178	0.00002	0.0045	4.6%
CS <sub>8</sub>	0.1103	0.1117	0.1036	0.1036	0.1103	0.1079	0.00001	0.0040	4.3%
CS <sub>9</sub>	0.1167	0.1177	0.1164	0.1099	0.1099	0.1141	0.00001	0.0039	4.5%
CS <sub>10</sub>	0.0595	0.0673	0.0671	0.0655	0.0655	0.0650	0.00001	0.0032	2.8%

## Acknowledgments

Financial support for this research was provided by the University of Peradeniya research grant (Research Grant No: URG/2017/26/E) and Peradeniya Engineering Faculty Alumni Association (PEFAA) in Australia.

The authors would like to express their sincere gratitude to the technical staff of the Department of Food Science and Technology, University of Peradeniya for providing required laboratory facilities. We would also like to show our gratitude to Eng. M. M. K. Sirisena, Former Workshop Engineer, Engineering Workshop, University of Peradeniya and all technical staff at Engineering Workshop, University of Peradeniya for their technical support.

## References

- Ahmad, a., Quegan, S., 2012. Analysis of maximum likelihood classification on multi-spectral data. *Appl. Math. Sci.* 6 (129), 6425–6436.
- Ashok, V., Agrawal, N., Durbanshi, A., Esteve-Romero, J., Bose, D., 2015. A novel micellar chromatographic procedure for the determination of metanil yellow in food-stuffs. *Anal. Methods* 7 (21), 9324–9330.
- Bandara, W.G.C., et al., 2018b. A multispectral imaging system to assess meat quality. In: 2018 IEEE Region 10 Humanitarian Technology Conference (R10-HTC) (R10 HTC'18).
- Bertelli, D., Plessi, M., Sabatini, A.G., Lolli, M., Grillenzoni, F., 2007. Classification of Italian honeys by mid-infrared diffuse reflectance spectroscopy (DRIFTS). *Food Chem.* 101 (4), 1565–1570.
- Bhatt, S.R., 2015. Impact Analysis of Food Adulterants on Health in Some Selected Urban Area of Varanasi.
- Bouzabata, A., 2019. Microscopic Analysis of Curcuma Longa L. Using Multivariate Test. pp. 2–7 no. March.
- Chainani-wu Nita, M., D.M., D., M.P., H., 2003. “Safety and anti-inflammatory activity of Curcumin: J. Altern. Complement. Med. 9 (1), 161–168.
- Daniells, S., 2018. Adulterated Turmeric Found in Supermarket Chainsquos Sample.
- Dhakal, S., Chao, K., Schmidt, W., Qin, J., Kim, M., Chan, D., 2016. Evaluation of turmeric powder adulterated with metanil yellow using FT-Raman and FT-IR spectroscopy. *Foods* 5 (2), 36.
- Duvoix, A., et al., 2005. Chemopreventive and therapeutic effects of curcumin. *Cancer Lett.* 223 (2), 181–190.
- Ennis, R., Schiller, F., Toscani, M., Gegenfurtner, K.R., 2018. Hyperspectral database of fruits and vegetables. *J. Opt. Soc. Am. A* 35 (4), B256–B266.
- Fuh, M.R., Chia, K.J., 2002. Determination of sulphonated azo dyes in food by ion-pair liquid chromatography with photodiode array and electrospray mass spectrometry detection. *Talanta* 56 (4), 663–671.
- Goel, M., et al., 2015. HyperCam. In: Proc. 2015 ACM Int. Jt. Conf. Pervasive Ubiquitous Comput. - UbiComp, vol. 15. pp. 145–156.
- Hoshino, K., Nielsen, F., Nishimura, T., 2007. “Noise reduction in CMOS image sensors for high quality Imaging: the autocorrelation function filter on burst image sequences ACF for image processing. *ICGST-GVIP* J. 7 (3), 3–10.
- Huang, L., Zhao, J., Chen, Q., Zhang, Y., 2013. Rapid detection of total viable count ( TVC ) in pork meat by hyperspectral imaging. *FRIN* 54 (1), 821–828.
- Jayaprakasha, G.K., Rao, L.J.M., Sakariah, K.K., 2002. Improved HPLC method for the determination of curcumin, demethoxycurcumin, and bisdemethoxycurcumin. *J. Agric. Food Chem.* 50 (13), 3668–3672.
- Joe, B., Vijaykumar, M., Lokesh, B.R., 2004. Biological properties of curcumin-cellular and molecular mechanisms of action. *Crit. Rev. Food Sci. Nutr.* 44 (2), 97–111.
- Khodabakhshian, R., Emadi, B., Khojastehpour, M., Golzarian, M.R., 2017. Determining quality and maturity of pomegranates using multispectral imaging. *J. Saudi Soc. Agric. Sci.* 16 (4), 322–331.
- Khulal, U., Zhao, J., Hu, W., Chen, Q., 2016. Nondestructive quantifying total volatile basic nitrogen ( TVB-N ) content in chicken using hyperspectral imaging ( HSI ) technique combined with different data dimension reduction algorithms. 197, 1191–1199.
- LWT - food Science and Technology Li, H., Chen, Q., Zhao, J., Wu, M., 2015. Nondestructive detection of total volatile basic nitrogen ( TVB-N ) content in pork meat by integrating hyperspectral imaging and colorimetric sensor combined with a nonlinear data fusion. *LWT - Food Sci. Technol. (Lebensmittel-Wissenschafts-Technol.)* 63 (1), 268–274.
- Lin, J.S., 1990. Two-dimensional Signal and Image Processing. Prentice-Hall, Inc., Upper Saddle River, NJ, USA.
- Liu, C., Hao, G., Su, M., Chen, Y., Zheng, L., 2017. Potential of multispectral imaging combined with chemometric methods for rapid detection of sucrose adulteration in tomato paste. *J. Food Eng.* 215.
- Lotlikar Chindarkar, Pranali, 2018. Sessions Court Upholds Action against Mumbai-based Firm for Food Adulteration.
- Manolakis, D.G., Lockwood, R.B., Cooley, T.W., 2016. Hyperspectral Imaging Remote Sensing: Physics, Sensors, and Algorithms. Cambridge University Press.
- Naz, S., Jabeen, S., Ilyas, S., Manzoor, F., Aslam, F., Ali, A., 2010. Antibacterial activity of Curcuma longa varieties against different strains of bacteria. *Pak. J. Bot.* 42 (1), 455–462.
- Porter, W.C., Kopp, B., Dunlap, J.C., Widenhorn, R., Bodegom, E., 2008. Dark Current Measurements in a CMOS Imager. 68160C.
- Prabhath, G.W.K., Bandara, W.G.C., Dissanayake, D.W.S.C.B., Hearath, H.M.V.R., Godaliyadda, G.M.R.I., Ekanayake, M.P.B., Demini, S.M.D., Madhujith, S.M.D., et al., 2019. Multispectral Imaging for Detection of Adulterants in Turmeric Powder. Optical Sensors and Sensing Congress (ES, FTS, HISE, Sensors), OSA Technical Digest (Optical Society of America, 2019) HTu3B.3.<https://doi.org/10.1364/HISE.2019.HTu3B.3>. In press.
- Radiometry, I.S., 2009. Technical Guide for Integrating Sphere Radiometry and Photometry, vol. 2001.
- Reibel, Y., Jung, M., Bouhifd, M., Cunin, B., Draman, C., 2003. CCD or CMOS camera noise characterisation. *Eur. Phys. J. Appl. Phys.* 21, 75–80.
- Richards, J.A., Jia, X., 1999. Remote Sensing Digital Image Analysis: an Introduction, third ed. Springer-Verlag, Berlin, Heidelberg.
- Ropodi, A.I., Panagou, E.Z., Nychas, G.J.E., 2017. Multispectral imaging (MSI): a promising method for the detection of minced beef adulteration with horsemeat. *Food Control* 73, 57–63.
- Ruby, A.J., Babub, K.D., Rajasekharan, K.N., 1995. Cancer letters. *Cancer Lett.* 94, 79–83.
- S. A. Screening and U. N. Spectroscopy, “Herb and Spice Safeguarding”.
- Sen, A.R., Sen Gupta, P., Chose Dastidar, N., 1974. Detection of Curcuma zedoaria and Curcuma aromatic in Curcuma longa (Turmeric) by thin-layer chromatography. *Analyst* 99 (1176), 153–155.
- Shafiee, S., Polder, G., Minaei, S., Moghadam-Charkari, N., van Ruth, S., Kuš, P.M., 2016. Detection of honey adulteration using hyperspectral imaging. *IFAC-PapersOnLine* 49 (16), 311–314.
- Shah, R., 2017. Identification and estimation of non-permitted food colours (metanil yellow and aniline dyes) in turmeric powder by rapid color test and thin layer chromatography. *World J. Pharm. Pharm. Sci.* 6 (8), 2034–2045.
- Sun, D.-W. (Ed.), 2010. “Copyright,” in *Hyperspectral Imaging for Food Quality Analysis and Control*. Academic Press, San Diego, pp. iv.
- van Raamsdonk, R.W.L.W.D., 2015. Microscopy for Fraud Detection.
- Vithana, S.S.P., Abeysekara, A.M.R., Oorloff, T.S.J., Rupasinghe, R.A.A., Herath, H.M.V.R., Godaliyadda, G.M.R.I., 2018. Comparison of two algorithms for land cover mapping based on hyperspectral imagery. 11 (1), 1–10.
- Yoo, Y., Lee, S., Choe, W., Kim, C.Y., 2007. CMOS image sensor noise reduction method for image signal processor in digital cameras and camera phones - art. no. 65020S. Proc. SPIE-Int. Soc. Opt. Eng. 6502.
- York, Timothy, 2011. Fundamentals of Image Sensor Performance.
- Zabalza, J., et al., 2014. Novel Folded-PCA for improved feature extraction and data reduction with hyperspectral imaging and SAR in remote sensing. *ISPRS J. Photogrammetry Remote Sens.* 93, 112–122.
- Zhang, L., et al., 2015. Determination of Dicyandiamide in Powdered Milk Using Direct Analysis in Real Time Quadrupole Time-Of-Flight Tandem Mass Spectrometry.